communications materials

ARTICLE

https://doi.org/10.1038/s43246-023-00401-3 OPEN

Operando tomographic microscopy during laser-based powder bed fusion of alumina

Malgorzata G. Makowska[1,2✉], Fabrizio Verga[3,4], Stefan Pfeiffer[5], Federica Marone[1], Cynthia S. T. Chang[6], Kevin Florio[3], Christian M. Schlepütz[1], Konrad Wegener[3], Thomas Graule[5] & Steven Van Petegem[1✉]

Laser-based Powder Bed Fusion (LPBF) of oxide ceramics enables fabrication of objects with complex three-dimensional shapes. However, mechanical properties of dense LPBF-manufactured ceramics are poor due to large amount of structural defects. Here, we perform the operando tomographic microscopy during LPBF of a magnetite-modified alumina to gain a deeper understanding of the underlying mechanisms. The effect of the laser energy density on the surface roughness, powder denudation zone and porosity formation mechanisms are investigated. Increasing laser power results in significant increase of the melt pool width, but not its depth and no melt pool depression is observed. Forces due to the recoil pressure are not seen to significantly influence the melt pool dynamics. Increasing power allows to avoid fusion porosity but enhances formation of spherical porosity that is formed by either reaching boiling point of liquid alumina, or by introducing gas bubbles by injection of hollow powder particles into the liquid.

---

[1] Photon Science Division, Paul Scherrer Institut, Forschungsstrasse 111, 5232 Villigen PSI, Switzerland. [2] Laboratory for Nuclear Materials, Paul Scherrer Institut, Villigen, Switzerland. [3] Institute of Machine Tools and Manufacturing, ETH Zurich, 8092 Zurich, Switzerland. [4] Inspire AG, Fürstenlandstrasse 122, 9014 St. Gallen, Switzerland. [5] Laboratory for High Performance Ceramics, Empa—Swiss Federal Laboratories for Materials Science and Technology, 8600 Dübendorf, Switzerland. [6] Technology Transfer Centre for Advanced Manufacturing, ANAXAM, 5232 Villigen PSI, Switzerland.
✉email: malgorzata.makowska@psi.ch; steven.vanpetegem@psi.ch

Additive manufacturing (AM) offers unique design freedom in the fabrication of complex three-dimensional shapes. Consequently, in recent years, AM technologies have expanded into multiple sectors, such as aerospace, automotive industry[1,2] and medicine[3]. One of the already commercialized AM techniques for metals and polymers is Laser-based Powder Bed Fusion (LPBF). In LPBF, parts are built up by sequentially adding precursor powder layers, followed by their selective consolidation by means of a laser, resulting in the densification of consecutive slices of a three-dimensional object[4]. The success of LPBF for producing metallic components with complex shapes has motivated scientists to investigate the possibility to use this technique for net shape ceramic parts, as their machining and shaping using conventional methods is challenging, time consuming and expensive due to their hardness and brittleness. However, laser-based AM of oxide ceramics implies additional challenges as compared to metals due to their significantly higher melting temperature, high viscosity, poor thermal shock resistance and poor absorption of laser light, as it is demonstrated in literature on LPBF of alumina[5–10] and zirconia[9,11,12]. The latter challenge can be well mitigated by introducing light absorption additives, such as carbon[6,13,14], titanium carbide[10,15] or other metal oxides[16–19]. However, the issue of structural defect formation, such as pores and cracks, which is related to the extreme temperature gradients from high heating and cooling rates combined with low heat conductivity and high Young's modulus, remains unsolved. The type and amount of defects as well as the final morphology of the samples depend strongly on the powder properties[20] and the laser scanning parameters such as laser power, scanning speed, laser spot size and hatch distance[21]. This dependence as well as effects of post processing have been widely studied, mainly based on simulations[22–25] and ex situ characterization techniques, such as XRD[5,17,26], optical[27] and electron microscopy[19,28]. The effect of laser parameters on roughness, porosity and other structural defects is frequently investigated after manufacturing using X-ray[19,29–31] and neutron[32] tomography.

The manufacturing of defect-free, high performance materials requires understanding of defect formation mechanisms and microstructural development as a function of process parameters. For that purpose, multiple in situ and operando techniques have been developed. This includes, for instance the observation of sputter formation using a high-speed camera[33], IR imaging[34], or two wavelength high-speed-imaging thermography to measure operando thermal gradients and cooling rates during LPBF[35].

In particular, operando techniques for LPBF process studies have been developed worldwide at synchrotrons, providing direct "live" insight into this complex manufacturing process[36]. This is reflected by numerous recent publications from such facilities, as the Swiss Light Source (SLS)[28,37–40], Stanford Synchrotron Radiation Light source (SSRL)[41–43] Diamond Light Source (DLS)[44–46], European Synchrotron Radiation Facility (ESRF)[47] and the Argonne National Laboratory's Advanced Photon Source (APS)[36,48].

Operando and in situ diffraction studies performed during LPBF allow for observation of phase transformations occurring prior and after melting and solidification as well as evaluation of temperature profiles and cooling rates[37,39,40,49], while in situ X-ray radiography provides invaluable knowledge about melt pool dynamics[49–52] and formation of defects such as cracks[39,53] and porosity[51,54,55]. Thanks to the rapid progress in detector and synchrotron development, X-ray radiography benefits from a high temporal resolution allowing frame rates up to 5 MHz[56] suitable for observing fluctuations of the keyhole, sputtering or powder particles ejection[57]. For metals, high-speed X-ray radiography studies, have shown that porosity formation mechanisms are strongly dependent on the melt pool dynamics. Pores can be formed because of keyhole fluctuation and due to trapping pores at the end of a scanning track when the laser is turned off[22,24,43] or because of a lack of fusion. Keyhole pores typically have a high sphericity and are directly linked to the specific melt pool shape attributed to too high energy density. In contrast, lack of fusion results in elongated, irregularly shaped pores, which depend on the melt pool size, scanning pattern and wetting process between the substrate and the liquid phase.

However, not all phenomena occurring during the LPBF process can be observed with 2-dimensional imaging, because X-ray radiographic imaging provides a signal averaged over the penetration depth. Therefore, radiography must be recorded only for thin samples (usually of the order of 0.4 mm) even for X-ray energy ensuring higher penetration depth, because of the poor contrast.

Operando radiography of LPBF is usually performed during one or a few laser tracks scanned perpendicular to the X-ray beam. In such measurements, it is not possible to spatially separate features along the beam direction, and thus, to link their location to the current laser position or to observe the interaction between scanning tracks. For such experiments, there is no powder on the side of the printed walls, but only at the top. In case of tomography, powder is in the x-ray beam path is not an issue.

Many features, such as cracks or non-spherical pores can be detected only if they are well aligned with the X-ray beam. Moreover, any movement of liquid phase pores or powder particles, as well as crack propagation, can be observed only if it occurs parallel to the image plane.

In contrast, tomographic microscopy, a 3D imaging technique, allows to see defects that are oriented in any direction as well as to observe their motion in all directions. Single scan lines can be clearly distinguished and it is possible to distinguish between material being deposited during the imaging, and material that was solidified during deposition of the previous layer. Some advantages of 3D imaging in additive manufacturing were demonstrated by tomography studies performed before and after laser scanning single layers at ESRF[48]. Thus, 3D imaging provides more detailed insight into the dynamic changes of the morphology allowing for observation of defect formation in the whole 3-dimensional manufactured object, which is more representative for the real process.

4D imaging, i.e., time-dependent 3D imaging, offers additional advantages. For instance, many microstructural features can be tracked by various ex situ techniques. However, only 4D imaging allows for the simultaneous observation of the various processes that led to these features, providing a deeper inside into their interplay.

Performing fast tomographic imaging is much more complex and challenging than radiography, since the observed object has to rotate during acquisition. Recent developments of synchrotron tomographic microscopy enabled ultrafast measurements allowing for 3D investigation of dynamic processes[58–60]. Currently the highest reported time resolution of tomographic microscopy is 1000 tps (tomograms per second)[58], which required a rotation of a sample with a frequency of 500 Hz.

Laser scanning speeds during LPBF of ceramics are in range from 1 to 100 mm/s[10,15,19,61], which is compatible with the current state-of-the-art fast 4D imaging. Indeed, at a laser scanning speed of 10 mm/s and an acquisition rate of 1000 tps, the laser spot moves by only 10 µm between each tomogram. For this range, the achievable tomogram rate is already compatible with typical laser velocities for ceramics, as for instance for 10 mm/s laser scanning speed and acquisition with 1000 tps, the laser spot would move by 10 µm during acquisition of one tomogram. Thus,

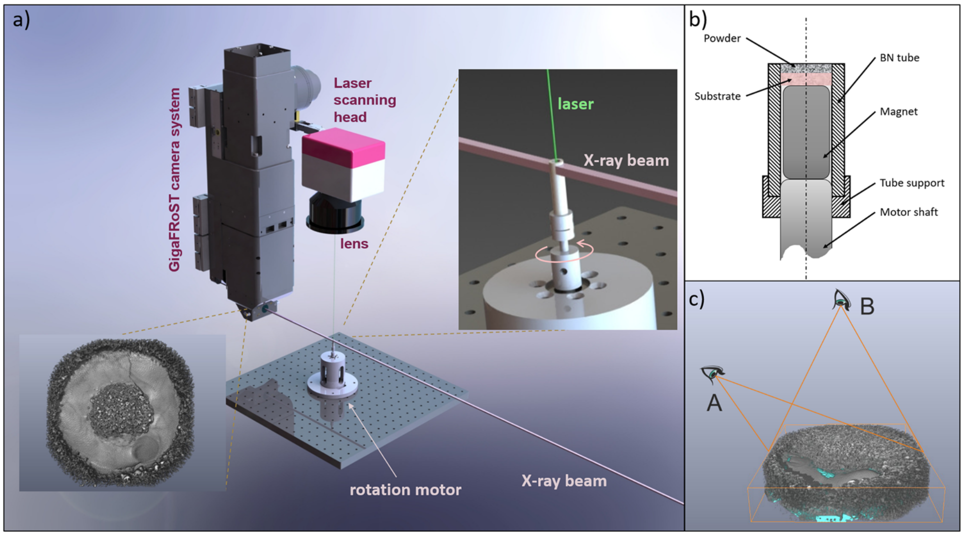

Fig. 1 Setup for operando tomographic microscopy during LPBF of ceramics. **a** Schematic of the LPBF device, **b** schematic of the rotational stage shaft with a boron-nitride (BN) tube containing the sample substrate, processed sample and the powder layer deposited on top of the sample; **c** schematic showing two perspectives A and B of 3D visualization of the powder bed used in following figures.

these parameters would allow to directly link the appearance of certain features with the melt pool dynamics. However, rotating turning a sample including the powder bed at such a high-speed induces centrifugal forces large enough to affect the powder stability. This severely limits the maximum achievable time resolution.

In this paper, we present a new method, based on magnetism, to assure powder stability during high-speed rotation, which allows to perform operando tomographic microscopy experiment during LPBF of a magnetite-modified alumina with a temporal resolution of 100 tps. The presented experiments allowed for real time 4D visualization of a melt pool and for observation of its dynamics. Moreover, these results provide an insight into processes underlying the structural defect formation.

Results

Operando X-ray tomography during laser powder bed fusion. In order to visualize the microstructure evolution in 3D during LPBF, operando X-ray tomographic microscopy experiments were performed on the TOMCAT beamline at the Swiss Light Source (SLS) (Fig. 1). A 20 W pulsed laser with a wavelength of 532 nm and a pulse duration of 1.5 ns was focussed to a spot size of 135 µm on the powder bed. Successive powder layers of 40 µm were deposited onto the substrate mounted inside a 3 mm boron-nitride cylinder. A permanent magnet mounted below the substrate counteracts the centrifugal forces experienced by the powder during rotation of the cylinder.

The scanning pattern was composed of 5 concentric circles with a 200 µm hatch spacing, resulting in cylindrical samples of 2 mm diameter. The powder consisted of spray-dried granules composed of micron and submicrometer size α-alumina particles with 5.2 vol% magnetite nanoparticles, which was confirmed with XRD analysis. The specification of the granules is summarized in Fig. 2.

While laser processing, the sample rotates at a speed of 50 Hz. For each concentric circle, the laser scanning speed is adjusted such that the relative speed of the laser spot on the powder bed was 2 mm/s. Simultaneously, X-ray images were recorded at a framerate of 20 kHz and 45 µs exposure time. For the reconstruction of the tomograms, the images were sorted into blocks of 200 projections acquired in a range from 0° to 180° and from 180° to 360° resulting in an effective frame rate of 100 tomograms per second (tps).

Effect of laser power on the surface roughness and balling effect. Various samples were manufactured with powers ranging between $P = 3.35$–15.5 W, corresponding to volume energy densities of 310–1435 J/mm^3. Movies showing the evolution of the powder bed and the solidified layer during laser processing are provided in Supplementary Movies SM1–SM8. Figure 3 shows six representative snap shots for selected powers ($P = 3.35$, 7.4 and 14.5 W). The perspective chosen for these images is indicated in Fig. 1c, as the position "A". The visualization is created as volume rendering with contrast corresponding to the attenuation coefficient of the X-ray beam. The color map, the view angle, as well as and the light and shadowing used for this rendering were adjusted to enhance the visibility of the surface roughness. The color scale corresponds to the linear attenuation coefficient, which depends on the density of the studied material. The sectioned material appears in red, while the material surface appears in green due to the partial volume effect at the surface. The laser scanning pattern starts from the inner ring for the samples manufactured with 3.35 and 7.4 W and from the outermost ring for the 14.5 W sample.

At $P = 3.35$ W, the low energy density results in lower temperatures, which leads to melting of small volumes of powder that solidify quickly in the form of spherical features. This effect is caused by the surface tension, which is inversely proportional to the temperature[22] and by insufficient wetting of the material of the previous layer. In Supplementary Movies SM1 (3.35 W), SM2 (4.3 W) and SM3 (5.2 W) it can be seen that the size of the "balls" grows with increasing laser power and eventually for 6.3 W balling disappears, though a significant surface roughness is still observed. Further increase of power leads to smoothing of the surface, as observed in Fig. 3 at $P = 14.5$ W and Supplementary Movie SM8.

Effect of laser power on powder denudation. Figure 4 presents selected time frames during processing of a single ring with laser powers of 7.4 W and 15.5 W observed in the perspective illustrated by the position "B" in Fig. 1c. Images "before laser scan" in Fig. 4 show the surface generated after solidification of the previous layer but before powder deposition (dark green for 7.4 W

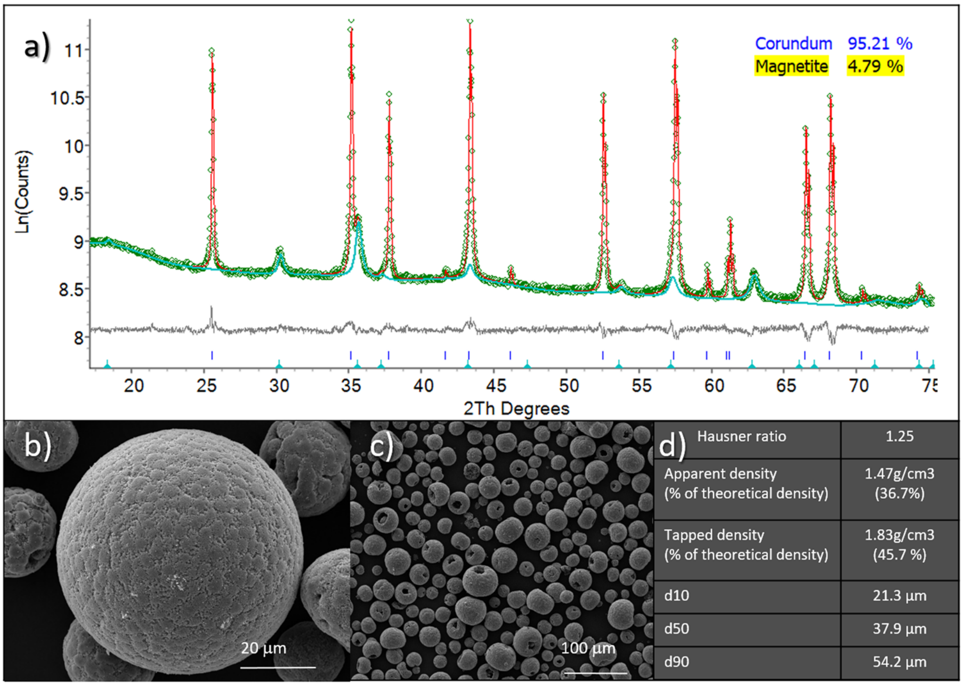

Hausner ratio	1.25
Apparent density (% of theoretical density)	1.47g/cm3 (36.7%)
Tapped density (% of theoretical density)	1.83g/cm3 (45.7 %)
d10	21.3 µm
d50	37.9 µm
d90	54.2 µm

Fig. 2 Powder characterization by XRD and SEM. a Diffraction pattern of the powder: red line is the fitted curve to the experimental data (green markers). The turquoise line shows fitting of the magnetite phase; **b**, **c** SEM images of the alumina granules with 5.2 vol% of magnetite; **d** macroscopic properties of the starting powder.

and cyan for 15.5 W). Images corresponding to the subsequent time frames were obtained by overlapping the surface generated for the previous layer and volume rendering of the sample in the currently observed state, composed of the solidified part and the powder. During processing with a power of 15.5 W, the surface of the previous layer is partly visible (as witnessed by the cyan areas surrounding the melt pool), indicating the absence of both powder or newly deposited material. This effect is caused by powder denudation. Close inspection of this process in individual frames demonstrates that the denudation zone is present both in front and at the side of the melt pool. This shows that, after stabilization of the melt pool, the laser beam does not interact with the powder directly, but rather with the melt pool itself. Strong denudation is very well visible in Supplementary Movie SM10, showing the operando process presented in Fig. 4 for 15.5 W, but also in Supplementary Movies SM7 and SM8 obtained for slightly lower laser power values, 13.2 W and 14.5 W, respectively. At even lower energy densities, the molten phase front remains in contact with the powder. At the lowest power the laser interacts directly with the powder (Supplementary Movies SM1 and SM2 for 3.35 W and 4.3 W). A similar effect was observed by Florio et al.[61] using a high-speed camera. Here, the energy density was varied by changing laser scanning speed, while keeping a constant laser power. It should be noted that the observation of the powder denudation for higher laser power is slightly affected by the rotation motion in the beginning of the scan. Namely, it can be observed that during the first 0.35 s after beginning of the laser scan, the denudation appears stronger on the inner side of the ring track than on the outer side (Fig. 4 0–0.35 s for 15.5 W).

The line plots in Fig. 4 present the evolution of the melt pool width (red data points) and the width of the denudation zone (blue data points) as a function of time. At 7.4 W, the laser track width (or denudation zone width) has a median of (372 ± 42) µm, which is significantly narrower as compared to the track formed at 15.5 W, with a width of (545 ± 50) µm. The median values obtained for the melt pool width are (213 ± 38) µm and (292 ± 25) µm at 7.4 W and 15.5 W, respectively. Both the median values and the standard deviations were evaluated for the measurements shown in Fig. 4 after melt pool stabilization, while excluding the values at the end of the laser scan.

3D visualization of the melt pool. Figure 5 compares representative 3D renderings of the melt pool for laser powers of 7.4 W and 15.5 W. The density of solid alumina at its melting point is 3.73 g/cm^3, while for liquid alumina at its melting point it is 3.05 g/cm^3,[62]. This difference allows segmentation of the liquid (dark gray) and solid phase (light gray due to its higher density), The samples processed at 15.5 W exhibits smooth and flat layers and a stable melt pool, which facilitates the material segmentation process. In contrast, the significantly higher surface roughness of the sample processed at 7.4 W leads to an unstable melt pool, which makes the segmentation process more challenging.

Figure 5 displays the volumes that have been selected for material segmentation as well as surfaces generated for the segmented liquid (green) and solid (purple) for 7.4 W (Fig. 5a–d) and 15.5 W (Fig. 5e–i). Volume rendering for the selected volume elements displayed together with overlapping surface indicating the border of the liquid, show that for both power values the segmentation corresponds well with the gray scale contrast.

The sample processed at 15.5 W exhibits a melt pool length of 517 µm (measured for the time frame in Fig. 5e, tangentially to the laser scan track), a width of 440 µm and a depth of 91 µm. Figure 6 shows a visualization of the melt pool development during the same laser scan over 100 ms. The average volume of the liquid phase show for the presented time frames is 8.7.10^6 ± 0.4.10^6 µm^3, demonstrating high stability of the melt pool size in time. At 7.4 W, the melt pool has a width of 240 µm, a depth varying between 30–60 µm and a total volume of 1.7.10^6 ± 0.2.10^6 µm^3, which is significantly smaller compared to the melt pool obtained for 15.5 W.

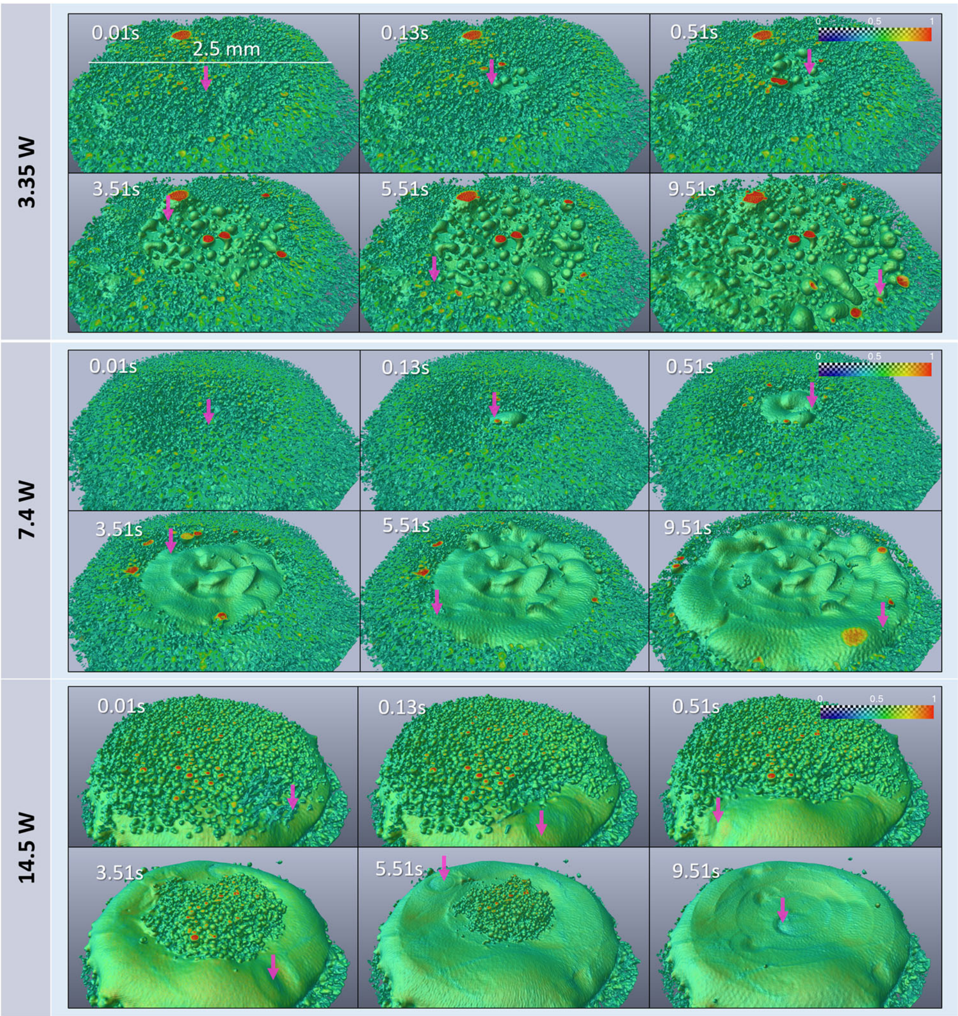

Fig. 3 3D visualization based on volume rendering of the powder bed during laser processing. The perspective is indicated in Fig. 1c, as the position "A". The color scale corresponds to the normalized linear attenuation coefficient. The sectioned material appears in red, while the material surface appears in green due to the partial volume effect. The pink arrows indicate the approximate laser position.

The shape of the horizontal (transverse) cross-section of the melt pool is round and not elongated (Figs. 5 and 6), in contrast to what is observed for LPBF processing of metals[22–25,34,37,43,63,64]. In the cross-section in the sagittal plane (vertical plane tangential to the laser scan track), the melt pool appears very shallow and broad.

Mechanisms of porosity formation. Two types of porosity could be detected: irregularly shaped lack-of-fusion pores and pores with a spherical morphology. Figures 7 and 8 show volume renderings and cross sections of samples processed with laser powers of 7.4 W and 15.5 W, respectively. For a low energy density corresponding to a power of 7.4 W, the wetting between the solid material (previous layer) and the liquid is poor. The liquid cannot penetrate grooves of the rough surface, leaving pores, as indicated by the pink arrows in Fig. 7d, e. The yellow arrow points to a lack of fusion porosity, where the process has started, and, apparently, there was poor wetting due to the low temperature of the previous layer.

Figure 8 shows a similar analysis for the sample processed with a laser power of 15.5 W. Also here, a lack of fusion at the start of the laser track ($t = 0.05$ s, Fig. 8a–d) is observed due to a rising but still low temperature of the liquid (compared with melt pool after longer laser processing) and the large difference in temperature between the molten and solid material, as indicated by pink arrows. At $t = 0.75$ s, the initial molten volume has spread over a larger area and the melt pool becomes wider and shallower. This is visible by comparison the cross-section at $t = 0.05$ s (Fig. 8c, d) with the cross-section at $t = 0.75$ s. (Fig. 8g, h). This can be ascribed to the increased temperature of both layer and substrate, which results in a reduction of the viscosity and surface tension, hence improved wetting. Eventually, the melt pool partially penetrates the previous deposited layer, resulting in good fusion between the two layers. This is reached after 0.2 s laser scanning. Thus, for high energy density, porosity due to lack of fusion occurs only at the beginning of the laser track. On the other hand, pores with spherical morphology are observed appearing within the volume of the liquid (green arrow in Fig. 8c).

Figures 9 and 10 show a volume rendering of a cropped volume indicated by the pink frame in Fig. 8a for different time frames. For each time frame, an enlarged picture of the segmented pores observed in the liquified volume is added using different colors. Dark green is used for pores located in the previous solidified layer, while other colors are used for the pores observed at the different time frames of the final layer. These images allow following the evolution and removal of the porosity in the liquid volume. In the absence of a keyhole formation, there are two

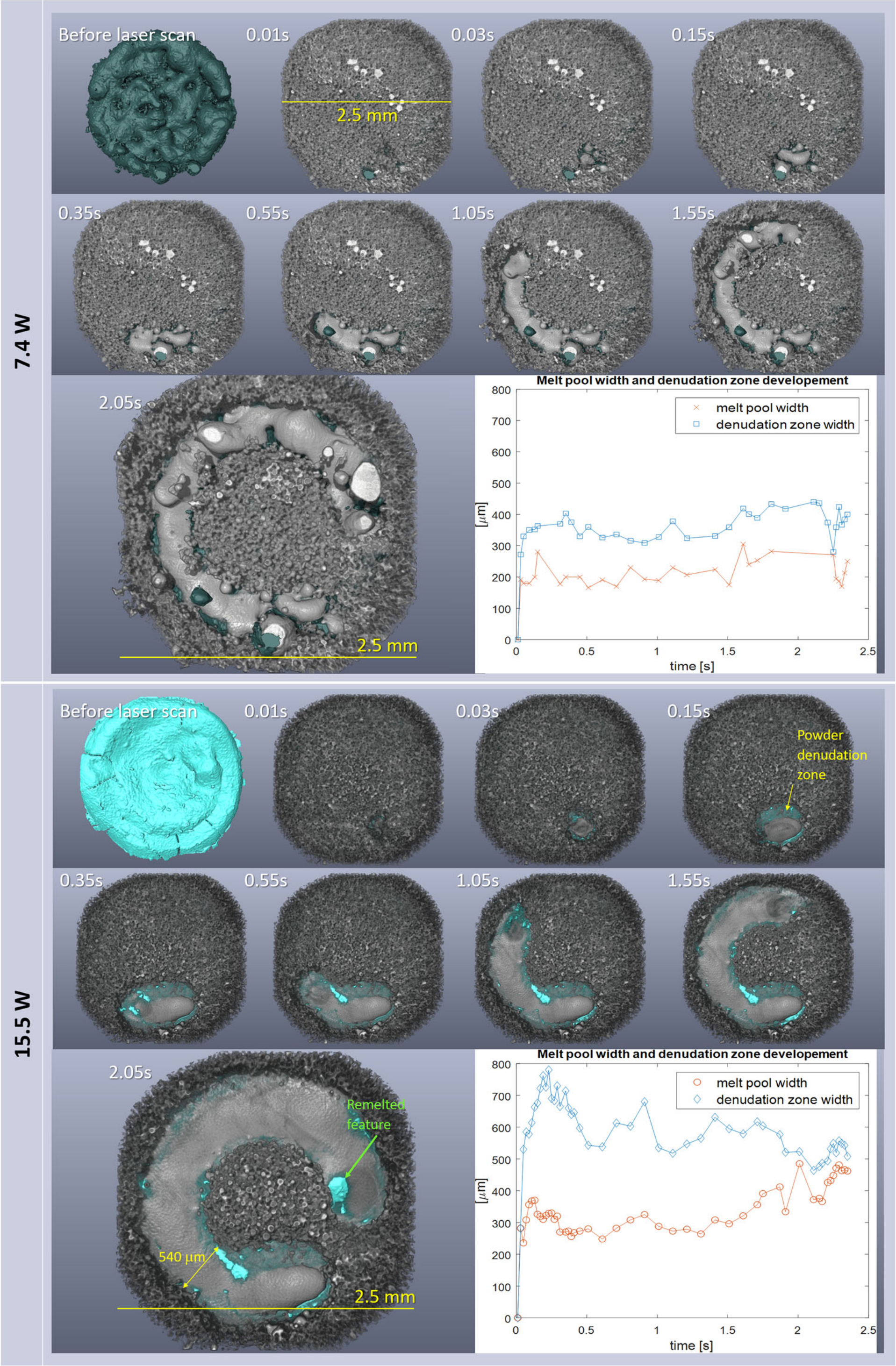

Fig. 4 Effect of laser power on the laser track width and powder denudation. The perspective is top view of the powder bed, as illustrated by the position "B" in Fig. 1c. Dark green and cyan illustrate the surfaces generated by solidification of the previous layer for 7.4 W for 15.5 W, respectively. The subsequent time frames are obtained by overlapping the surface of the previous layer and volume rendering of the sample in the currently observed state. Visualization of the last frame at $t = 2.47$ s does not contain the surface of the previous layer. Videos of the cross-section overview of the corresponding samples are presented in Supplementary Movies SM9 (for 7.4 W) and SM11 (for 15.5 W). The line plots present the change in time of the melt pool width (red data points) and the width of the denudation zone (blue data points) for the corresponding laser power.

possible mechanisms to create such pores: formation of gas bubbles and the presence of pre-existing pores inside the powder. The difference between the boiling point of alumina (2980 °C)[65] and its melting point (2072 °C)[65] is relatively low. Therefore, it is not unlikely that the boiling point is reached during laser processing, resulting in the creation of gas bubbles. On the other hand, SEM images of the powder (Fig. 2) reveal that some of the spray-dried granules, in particular the larger ones, are hollow. The injection of such granules into the melt pool can, therefore, result in gas bubbles within the liquid phase.

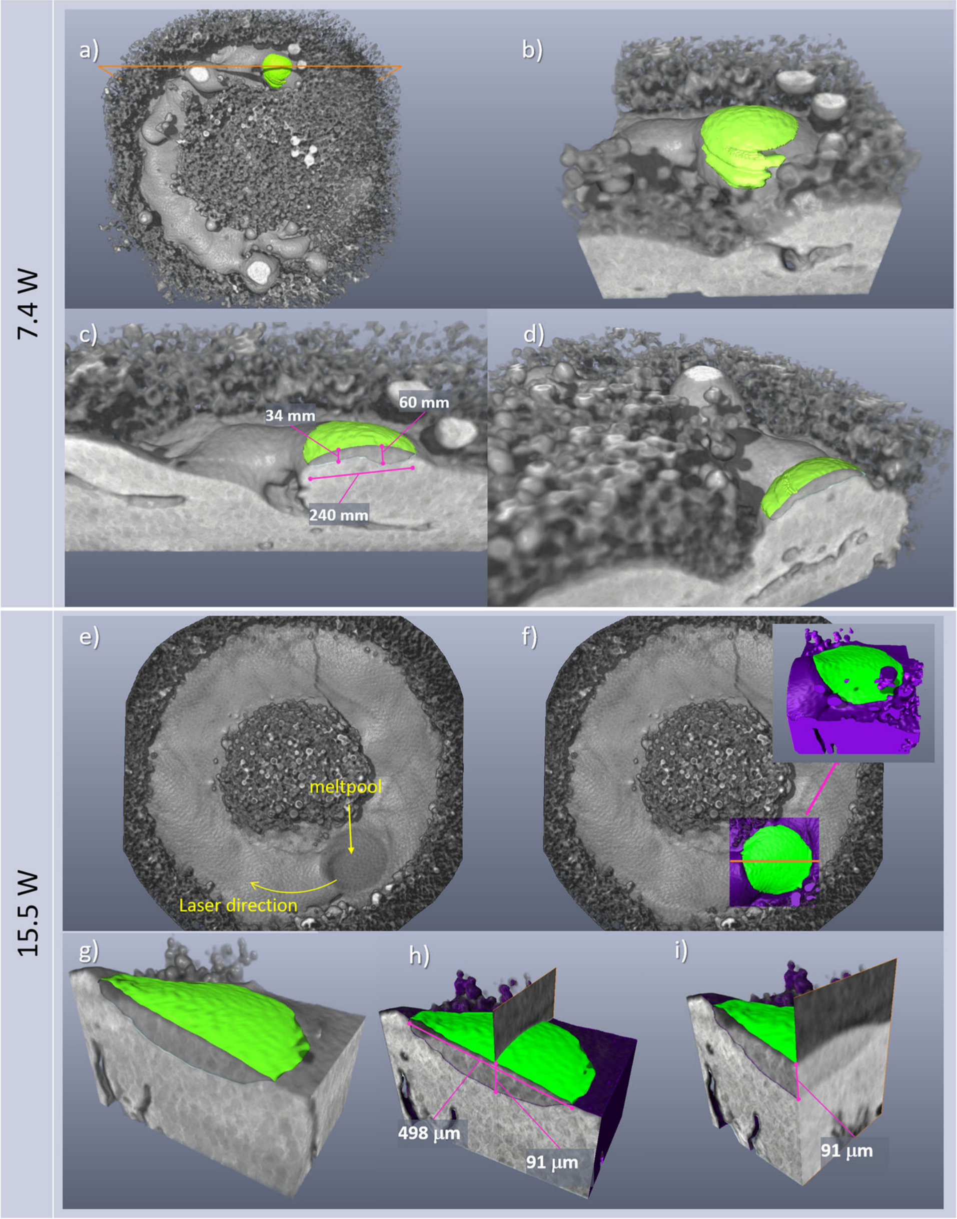

Fig. 5 Melt pool visualization for laser powers of 7.4 W and 15.5 W. Volume rendering of a sample processed with 7.4 W (**a** full sample volume; **b** cropped volume used for material segmentation; **c**, **d** cross sections trough the melt pool). Volume rendering of a sample processed with 15.5 W (**e**, **f** full sample, **g**–**i** cropped volume used for material segmentation with cross sections trough the melt pool). The orange frame in (**a**) indicates the position of the clipping plane presented in (**c**). The orange line in (**f**) indicates the clipping plane applied in (**g**–**i**). The surface of the material labeled as liquid is illustrated in green. Purple corresponds to the solid phase for 15.5 W. The gray scale corresponds to the linear attenuation coefficient.

The bubbles observed in this experiment typically appear with diameters between 10–40 µm. However, also larger pores can be formed, due to the coalescence of bubbles that appear close to each other, as it is illustrated in images for $t = 0.05$, 0.06 and 0.07 s. Most of the pores that appear inside the liquid move toward the surface and escape. This is illustrated by the green arrows in Fig. 9 for $t = 0.12$ s and $t = 0.13$ s. However, in some cases the bubbles are trapped by the solidified material and remain as residual pores.

Figure 10a presents the pore formation, after the melt pool has stabilized, where it becomes wide and penetrates the material of the previous layer. In the consecutive time frames, gas bubbles frequently emerge. The vast majority of them appear at the edge of the melt pool, mostly at its front, where the temperature is highest, and the boiling point is most likely to be reached. Some pores show up at the side of the melt pool (relative to the scanning direction). This suggests that these gas bubbles are introduced by the granules dragged into the molten phase. It should be noted that with 2D imaging it is not always possible to distinguish whether the bubbles appear on the side or in the center of the melt pool.

Figure 10b shows the evolution of the spherical type of porosity in the same volume of the sample presented in Figs. 9 and 10a, taking into account both porosity created in the material during deposition of the previous layers and the porosity appearing during the current laser scan. The blue data points represent the maximum of the equivalent diameter of the pores existing in the corresponding time frame. The red data points correspond to an average equivalent diameter and the yellow show the number of pores observed in a current time frame.

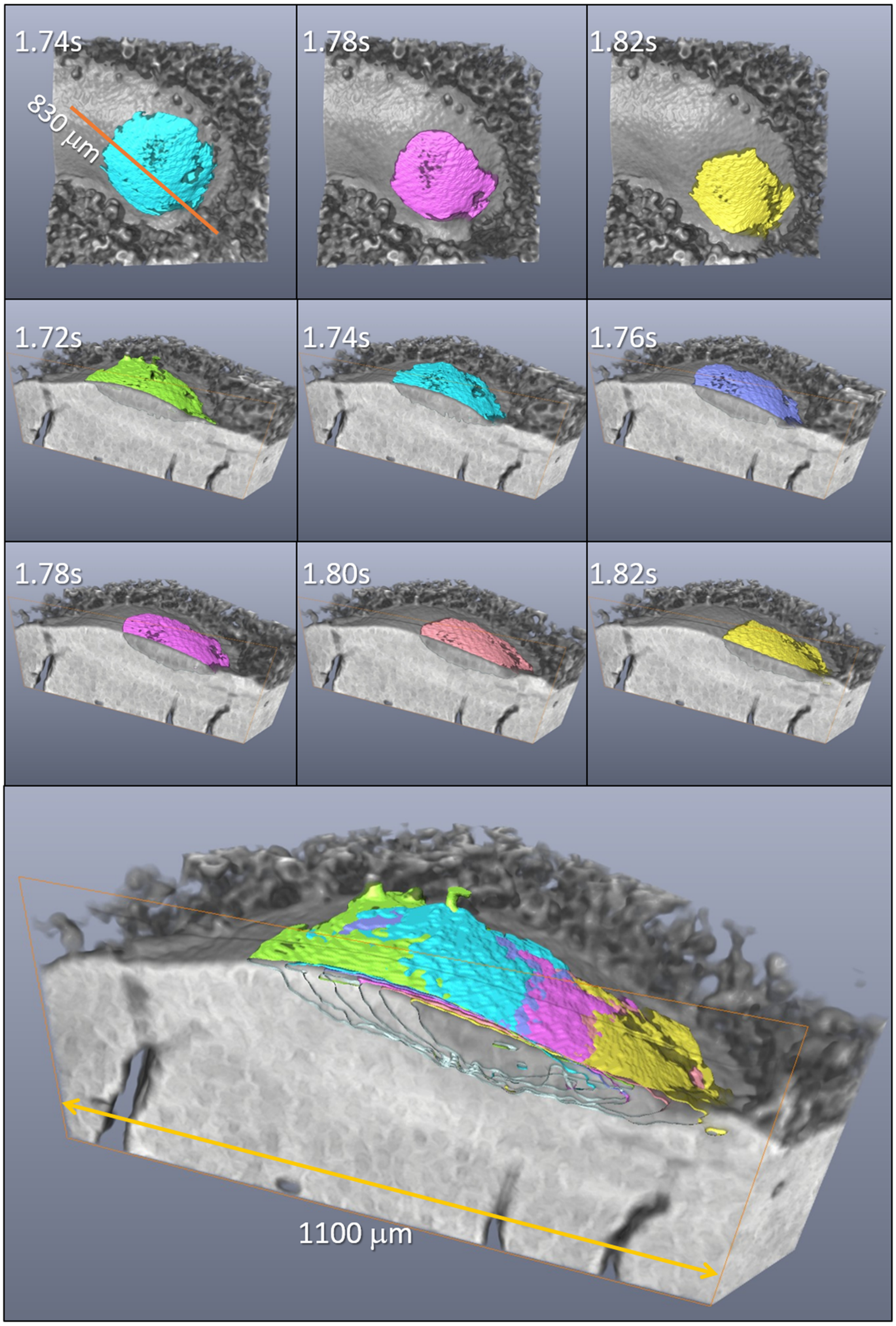

Fig. 6 Melt pool evolution visualization for subsequent time frames for 15.5 W. The first 3 panels illustrate the top view. The plane indicated by the orange line clips the volumes presented in perspective. Bottom picture is the superposition of the situations at different time steps. The colors correspond to specific time frames.

Discussion

In this study, the effect of laser power on the surface roughness, powder denudation, melt pool development and porosity formation mechanisms in LPBF processing of magnetite-modified alumina was investigated. It was observed, that very low laser power, and therefore insufficient energy density, leads to the absence of a powder denudation zone and hence a direct interaction between laser and powder and to melting a relatively small volume of the powder. The reached temperature is relatively low and therefore the surface tension and viscosity is high, leading to balling and significant surface roughness. In such cases, also poor wetting between the liquid phase and solid part is observed, which together with high roughness leads to significant porosity formed due to lack of fusion between consecutive layers.

Increasing the energy density results in higher temperatures and in the formation of a powder denudation zone around the laser track. As a consequence, the laser light interacts directly with the melt pool, and not with the powder. A larger amount of liquid phase is obtained and higher temperatures in the melt pool are reached. This, together with an increase of temperature of the

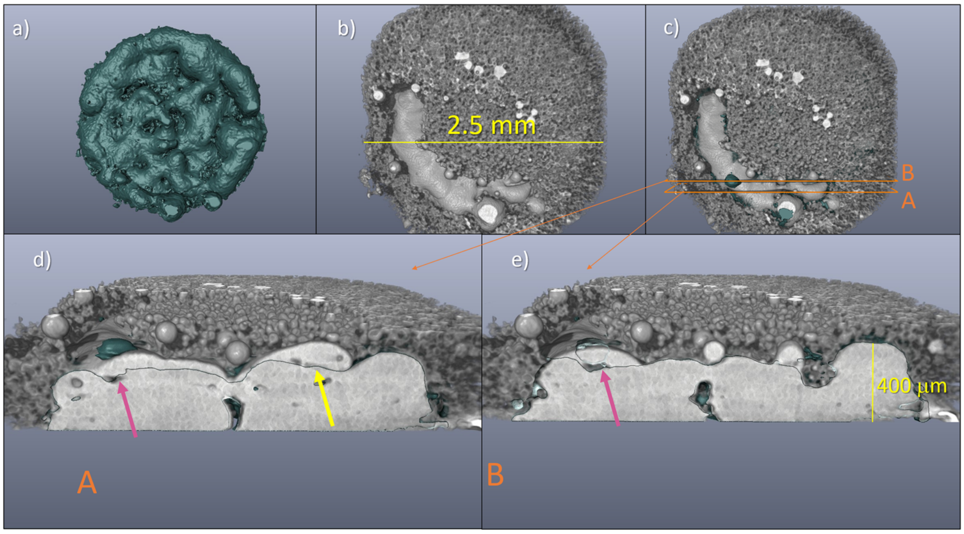

Fig. 7 Porosity caused by lack of fusion between consecutive layers due to poor wetting for the sample processed with a power of 7.4 W. a Surface generated after solidification of the previous layer, **b** a volume rendering of the partially processed new layer at $t = 0.75$ s. In (**c**), the planes A and B are indicating the cross sections shown in (**d**) and (**e**). These images are a combination of the surface generated after solidification of the previous layer shown in (**a**) and a volume rendering of the sample after $t = 0.75$ s. Thus, the cross sections shown in (**d**) and (**e**) show the situation shortly after solidification of the material with a visible contour of the surface of the previous layer. The video in Supplementary Movie SM9 presents the corresponding cross sections.

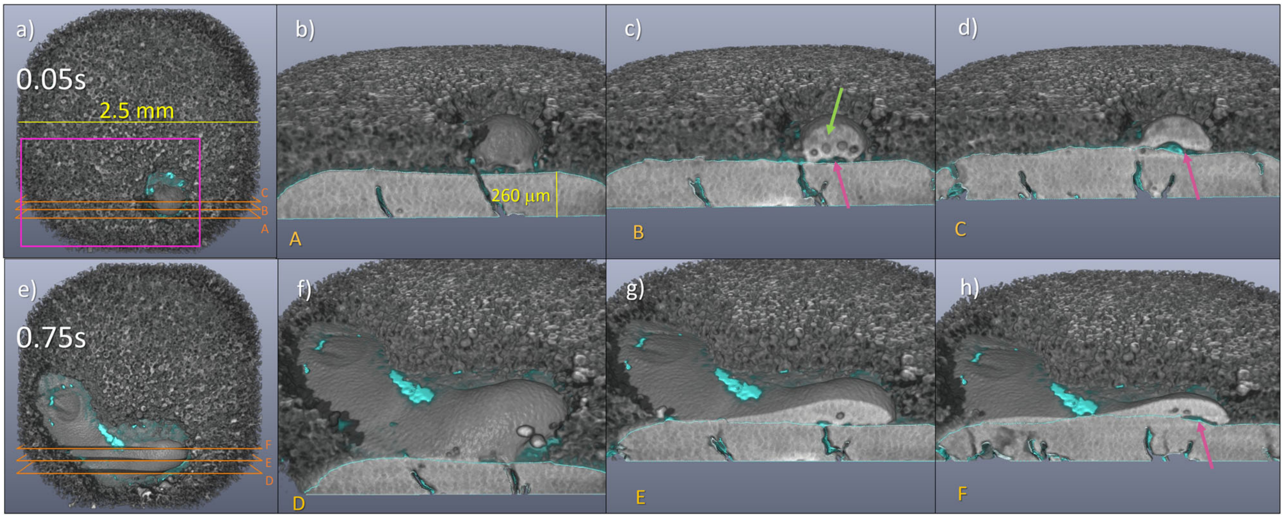

Fig. 8 Porosity due to volume evaporation and lack of fusion for a sample processed with a power of 15.5 W. a Volume rendering at $t = 0.05$ s, including the position of the planes A, B, and C for which the cross sections are shown in (**b–d**). **e** Volume rendering at $t = 0.75$ s and the planes D, E and F for which the cross sections are visualized in (**f–h**). The video in Supplementary Movie SM11 presents the corresponding cross sections.

surrounding material, decreases surface tension and improves wetting, and consequently leads to a smoother surface and elimination of the porosity associated with lack of fusion. It is clear that the formation of the powder denudation zone and consequently creation of a melt pool on the substrate, with simultaneous powder feeding into the melt pool is a favorable mechanism. However, too high energy density leads to an excessive denudation, and in such a case, a vast amount of powder is consumed during scanning of the first laser track. It was observed that in case of a pattern composed of concentric rings, there was no powder available during scanning of the last ring in the pattern. This resulted in a smooth, but uneven layer with significantly higher edges, when scanning started from the outermost ring.

It was observed that the denudation zone is present both in front of and on both sides of the melt pool. This shows that the laser beam does not interact with the powder directly, but rather with the melt pool itself. The vapor jet created at the center of the melt pool causes a zone of reduced pressure because of the Bernoulli effect. This entrains ambient gas, thereby dragging surrounding particles into the melt pool, which results in a zone depleted of powder[33].

For laser power of 15.5 W both the melt pool width and denudation zone width are significantly larger than for power 7.4 W. Also the difference between melt pool and the denudation zone widths is larger for the higher power. In both cases it can be observed how the melt pool and denudation zone grow at the very beginning of the laser processing to reach certain size, which fluctuates over the laser scan, mainly due to roughness of the material below. Interestingly, the denudation shows even stronger fluctuations, especially in case of higher laser power. This is related to uneven surface resulting in uneven powder layer and

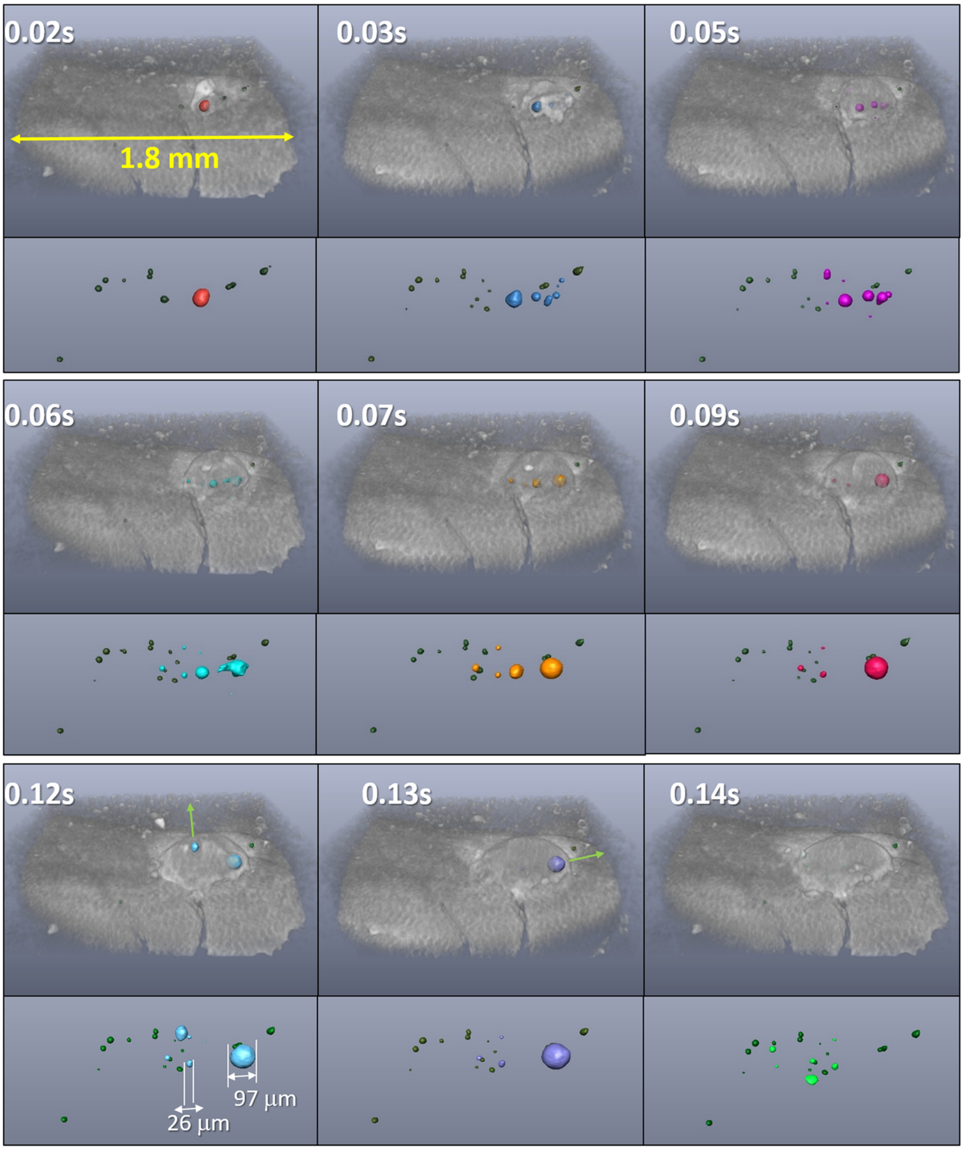

Fig. 9 Visualization of porosity appearing inside the molten material in the beginning of the laser scanning with power 15.5 W. The upper image of each time frame shows volume rendering of a cropped volume indicated by the pink frame in Fig. 8a with a gray scale adjusted the way that powder is almost transparent, the solid and liquid phase are visible, but with transparency allowing to see the pores close to the surface. The bottom image of each frame shows only the material labeled as porosity. Dark green corresponds to porosity in the solid material of the previous layer, while other colors illustrate the pores in the liquid.

ability to move larger amounts of powder due to stronger gas flow. It can be observed that for larger power, the melt pool size becomes larger in the end of the ring, which is a zone already depleted in powder.

4D imaging allows for quantitative analysis of the porosity evolution. High energy density eliminates the formation of lack of fusion porosity, except for the beginning of the laser scan, when the temperature of the melt pool and the substrate is still rising. On the other hand, for this case, more pores with spherical morphology were observed appearing within the liquid phase. Such spherical pores had been observed in previous ex situ studies, and due to their shape, it was expected that they could be related to the keyhole formation in the melt pool, however this study shows that it was not the case. It was observed that most of such bubbles float to the surface and escape, however, some bubbles can be trapped during solidification of the surrounding material, resulting in spherical porosity. As it can be seen in the plots in Fig. 10b, the average size of pores of this type is relatively stable, while the maximum size of pores significantly fluctuates. In the plot showing the maximum pore equivalent diameter changes as a function of time, we can observe sudden changes that can be associated with what is observed in the images. For instance, an increase of diameter at $t = 0.06$ s, when the coalescence of gas bubbles occurred, or sudden decrease at $t = 0.13$ s when the large gas bubble reached the surface of the liquid and could escape. The number of pores illustrated by the yellow curve in Fig. 10 shows that significant increase in porosity takes place mainly at the beginning of the laser scan, and once the melt pool is stabilized, in this case at about $t = 0.2$ s, there is no significant increase of the number of pores. This can be explained with the fact that after this time the melt pool is broad and shallow enough that almost all the gas bubbles escape to the surface of the liquid. At the beginning of the scan the molten volume has more roundish shape and the distance of the gas bubbles to the surface can be too large to escape before the solidification. Additionally, at the beginning of the laser scan the temperature is lower, which

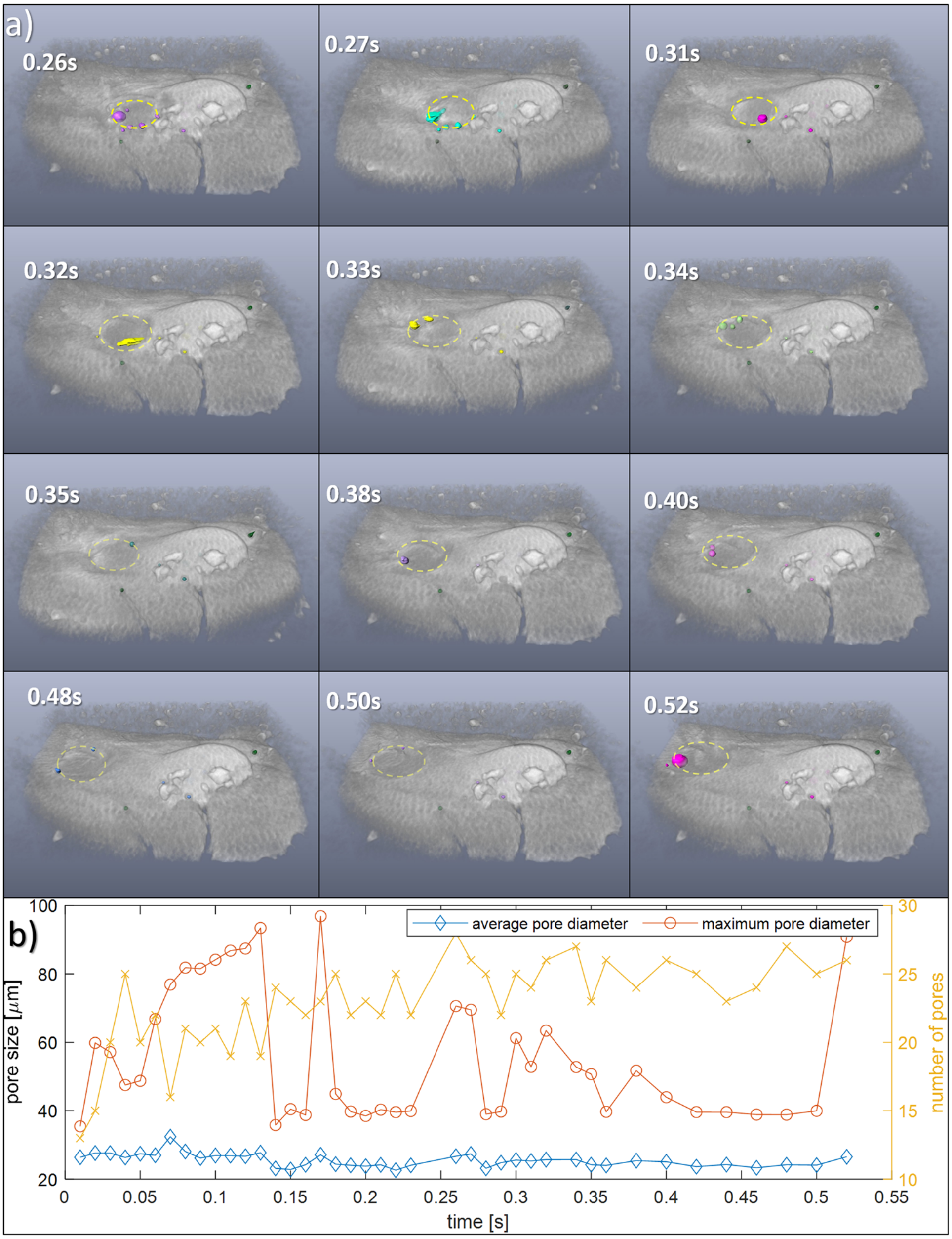

Fig. 10 Pore evolution at 15.5 W. a Visualization of porosity appearing inside the molten material after stabilization of the melt pool. Images show volume rendering of a cropped volume indicated by the pink frame in Fig. 8a with a gray scale adjusted the way that powder is almost transparent, the solid and liquid phase are visible, but with transparency allowing to see the pores close to the surface. Yellow contour indicates the melt pool position. Pores typically appear at the front of the melt pool and less frequently at its sides, but in both cases, close to the melt pool edge. **b** Porosity evolution during laser scanning time 0–0.52 s.

is associated with slightly higher surface tension and viscosity[66], additionally hindering the movement of the gas bubbles to the surface. This observation shows that this type of porosity in such conditions is produced mainly in the beginning of the laser scan.

Analysis of the melt pool shape for different laser powers revealed that increasing power leads to an increase of the horizontal melt pool size, but less to an increase of its depth. Remarkably, even for high energy densities up to 1435 J/mm^3 (for the used laser scanning parameters corresponding to the power of 15.5 W), the top surface of the melt pool remains relatively flat, and in the cross-section in the sagittal plane, the melt pool appears very shallow and broad, which is in contrast to simulations[22–24,54,67] and in situ 2D imaging experiments performed for metallic systems[34,52,54,63,68]. For metals, it was demonstrated that the dynamics of the melt pool and therefore its shape is defined by the recoil pressure, Marangoni convection, surface tension and buoyancy. The recoil force that appears after the liquid starts to evaporate is dominant[67] and causes depression of the melt pool, in other words a concave shape of the top surface. Increasing the energy density results in a stronger depression, which eventually leads to the creation of a keyhole. Given that the energy density is high enough, this occurs for metals regardless of the scanning speed, since similar effects have been described even for stationary experiments[69].

The energy density does not, take into account any material properties, therefore, an approach for the melt pool behavior prediction using a dimensionless parameter of normalized enthalpy was adopted for LPBF[70,71]. It was originally proposed by

Table 1 Material parameters used for calculation of the normalized enthalpy.

Parameter	Value	Comments
A	0.7–1	0.7 is the value measured for 1 vol% of iron oxide doping[5,17]
κ	7.5 W m^{-1} K^{-1}	Thermal conductivity at temperature close to the melting point[77,78]
ϱ	3.73 g cm^{-3}	Density of solid alumina at melting point[62]
ϱ_l	3.05 g cm^{-3}	Density of liquid alumina at melting point[62]
c	1.38 J g^{-1} K^{-1}	Specific heat capacity of solid alumina at temperature close to the melting point[79]
c_l	1.89 J g^{-1} K^{-1}	Specific heat capacity of liquid alumina at temperature close to the melting point[79]
T_m	2345 K	Melting temperature of alumina
T_b	3250 K	Boiling temperature of alumina

Hann et al. for prediction of the laser weld properties[72]. The normalized enthalpy ($\frac{\Delta H}{h_s}$) is described by the following formula: $\frac{\Delta H}{h_s} = \frac{AP}{h_s\sqrt{\pi D v \sigma^3}}$, where A is absorptivity, P is laser power, h_s is enthalpy at melting, D is thermal diffusivity of the molten material, σ is the laser spot radius (in this case 67.5 µm), and v is the laser scanning speed (2 mm/s). D can be calculated as $D = \frac{\kappa}{\varrho_l c_l}$, and $h_s = c(T_m - T_0)\varrho$. For the calculation of the normalized enthalpy and its threshold for the keyhole mode, the parameters of the material used in this work were assumed to be very close to pure alumina, except for the absorptivity. The used parameters and their values are summarized in Table 1.

According to the proposed criteria for the keyhole threshold[70]: $\frac{\Delta H}{h_s} > \frac{\pi T_b}{T_m}$, the keyhole mode for LPBF of alumina should occur for $\frac{\Delta H}{h_s} > 4.4$. However, even for the highest used power 15.5 W in this work, for which the $\frac{\Delta H}{h_s}$ is in range from 21.7 to 31 (assuming absorptivity in range from 0.7 to 1), still no keyhole was observed. This indicates that the proposed model does not apply in the case of the alumina and that the more universal model should include not only thermodynamical properties of material, but also thermophysical properties, such as viscosity and surface tension.

The lack of depression in the melt pool of alumina in the presented experiments indicates that the influence of the recoil pressure in this case is less pronounced. Cullom et al.[67] concluded that in case of stainless steel, the LPBF process operates in the conduction, transition and keyhole mode for recoil forces below 0.5 mN, between 0.5 and 8 mN, and above 10 mN, respectively. An experiment performed with a similar ceramic powder as in this experiment, and using a similar laser (532 nm, 1.5 ns pulse, 300 kHz repetition rate) with a power of 5.75 W, showed a much lower recoil force value of 0.018 mN, which was confirmed by simulations[73] and explains the lack of the melt pool depression in the studied system. The very low recoil pressure is in part due to the low duty cycle of 0.045% of the pulsed laser. In between pulses, the energy can dissipate over a large volume, resulting in the observed round shape of the melt pool. Moreover, the observed melt pool shape can be caused by either the significantly lower scanning speed and/or by the higher viscosity of molten alumina (about 30 mPa s[66]) compared to that of metal alloys (5 mPa s for steel[69], 1.3 mPa s for Al[74]). Similar effect of was observed by Leung et al.[46], who observed significantly smaller length and depth of the melt pool for high viscosity bioactive glass, as compared with low viscosity steel.

The above presented interpretation needs further investigation and a direct comparison with numerical simulations, together with crack evolution analysis, will be the scope of our further research. Moreover, the presented 4D experiments have a great potential to provide input needed for development of numerical modeling of the melt pool dynamics.

Methods

Material. The powder used in this study is composed of spray-dried granules produced from a bimodal mixture of micron and submicron sized α-alumina particles with 5.0 vol% of iron oxide nanoparticles in form of hematite (Spherical α/γ-Fe_2O_3, L2715D, BASF SE, Ludwigshafen, Germany) before reduction, which resulted in 5.2 vol% of magnetite after reduction. A detailed description of the process of powder synthesis can be found in ref. [17]. The addition of the iron oxide particles was found to improve laser absorptivity[5,16,17]. Before the LPBF processing, the granules were heated up in a reducing atmosphere to 500 °C with a heating rate of 5 °C/min and cooled down immediately after reaching the target temperature with the same rate. As a result, the hematite phase was reduced to magnetite. This was confirmed by an XRD measurement, performed in Bragg–Brentano geometry using a Bruker AXS D8 ADVANCE diffractometer with a Cu-Kα X-ray source. The data were acquired in a 2θ range of 10–100° with a step of 0.02° and 1 s exposure time per step. The TOPAS Bruker AXS software was used for identification of crystallographic phases, as presented in Fig. 2a.

At such a short processing time and low temperature, no sintering or significant morphology changes of the granules were expected. To confirm that, the shape of the granules and their microstructure were investigated by scanning electron microscopy (VEGA3 Tescan, Tescan instruments, Czech Republic). Figure 2b, c presents the structure and morphology of the granules after reduction, and Fig. 2d summarizes the properties of the powder after reduction.

LPBF setup and laser scanning strategy. The setup for operando tomographic microscopy during LPBF processing is equipped with a 20 W pulsed laser with a wavelength of 532 nm and a pulse duration of 1.5 ns (IPG GLPM-20, United States). A galvoscanner (Raylase, Germany) with an f-θ lens guides the laser beam to the powder bed placed on the sample stage. Figure 1 presents a simplified schematic of the setup, and Fig. 11 shows the setup mounted at the TOMCAT beamline. The pulse repetition rate was fixed to 300 kHz. The laser spot diameter used throughout the whole experiment was 135 µm and had a Gaussian profile, while the laser power was varied during the experiment. The powder layer thickness was 40 µm. The energy densities were calculated as $E = W/2rvd$, where W stands for the laser power, r is the laser spot radius, v the scanning speed and d the layer thickness.

The in-house built sample stage contains a rotation brushless DC-servomotor with an optical encoder purchased from FAULHABER MINIMOTOR SA and a boron-nitride (BN) tube with inner and outer diameters (ID and OD) of 3 mm and 5 mm serving as powder bed. A substrate in form of either alumina foam (70% porosity) or ex situ processed alumina part, is fixed on the shaft of the rotation motor inside the BN cylinder. The setup is equipped with a manual powder layer deposition system based on a manual stage with a precision of 2 µm. The scanning pattern was composed of 5 concentric circles with 200 µm hatch spacing, resulting in building cylindrical samples of 2 mm diameter. The laser scanning speed was 2 mm/s with respect to the sample. This

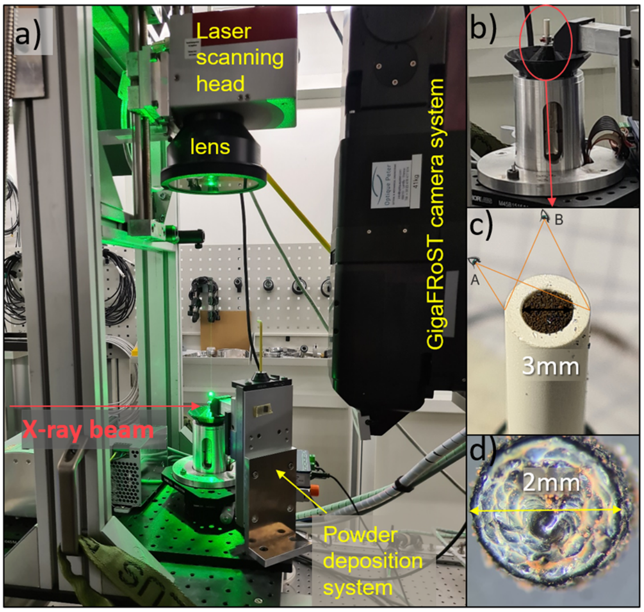

Fig. 11 Setup for operando tomographic microscopy during LPBF of ceramics. **a** The setup mounted at the TOMCAT beamline. **b** rotational stage with a boron nitride (BN) tube (the white tube marked in the red frame) containing the sample substrate, processed sample and the powder layer deposited on top of the sample; **c** magnified top view of the powder bed (the black material inside the tube is the magnetite-modified alumina powder); **d** an optical microscopy image of a sample manufactured during 3000 rpm rotation.

was the relative speed of the laser spot on the powder bed, meaning that for different ring diameters the actual laser spot was moving with different linear speeds that were equal to 2π*50 Hz*(ring radius) + 2 mm/s.

Obtaining high frame rate tomographic acquisition implies additional challenges due to the high-speed rotation of the system, which results in high centrifugal forces making it challenging to keep the powder bed stable. Since the powder used for the experiment exhibits a very good flowability, the risk of moving the powder to the edges of the cylinder due to the centrifugal forces had to be mitigated. First, the effect of centrifugal force is minimized by using a small (3 mm) diameter powder bed. Secondly, pilot studies showed that the maximum rotational speed, for which the powder inside the 3 mm ID tube remains stable, is in the range of 1300–1500 rpm (25 Hz). To further improve the acquisition frame rate, a small neodymium magnet (2.8 mm diameter, 5 mm high cylinder) was placed below the sample substrate (between the motor shaft and the substrate). The magnetic properties of the absorption additive in alumina powder in form of a magnetite allowed to increase the rotation speed to 50 Hz, while still keeping the powder bed stable. The magnetic field was kept as low as possible by adjusting the substrate thickness, to avoid its influence on the laser manufacturing process. The applied magnetic field was just enough to deposit up to 20 layers, after which it was too weak to keep the powder in place. The role of the magnetic field was crucial especially during the transient acceleration of the rotation motor, but its effect on the laser processing is negligible, because of the low Curie temperature of magnetite, which is 580 °C, and hence is far below the temperatures occurring during the laser processing.

Operando tomography. Operando tomographic microscopy was performed at the TOMCAT beamline of the Swiss Light Source (SLS) at the Paul Scherrer Institute. The polychromatic X-ray beam is generated by a 2.9 T bending magnet and filtered by 5 mm glassy carbon (Sigradur) and 1 mm Si to remove the low energy fraction. This minimizes potential beam hardening artefacts. The details of the beam spectrum can be found in ref. [60]. The projections were recorded by a detector setup composed of a 150 µm thick LuAG:Ce scintillator, a high numerical aperture macroscope (Optique Peter) with a ×4 magnification and the gigabit fast readout system for tomography (GigaFRoST camera) visible in Fig. 11a[75]. This in-house designed detector system allows for continuous data transfer at up to 7.7 GB/s to a data backend server enabling high-speed acquisition over an extended period of time. The effective pixel size was 2.75 µm and the field of view (FOV) was 912 × 180 (in pixels). The images were recorded during continuous sample stage rotation with 50 Hz, over up to 10 s with an acquisition rate of 20 kHz and 45 µs exposure time. During the experiments, the rotation motor was started prior to the laser scanning. Several seconds after reaching 50 Hz, the laser scan was started with sending a trigger at the same time to the camera to start the acquisition.

For the reconstruction, the images were sorted into blocks of 200 projections acquired in a range from 0 to 180 and from 180 to 360 resulting in 100 tomograms per second (tps). For this acquisition and a laser scanning speed of 2 mm/s, the laser spot moves by 20 µm per tomogram, which is significantly less than the laser spot size of 135 µm. For each set of laser parameters, data acquisition was performed several (minimum 3) times.

The achieved spatial resolution for static features, like cracks and porosity in solid material was below 10 microns. However, the spatial resolution of dynamic features depends on the speed of their movement. The resolution for observation of the melt pool is limited by the distance that it moves during acquisition of a full tomogram, which results in blurring of the liquid-solid interface over this distance.

Reconstruction and data analysis. The tomograms were reconstructed with the "gridrec" algorithm[76]. Further data reduction and analysis including material segmentation and visualization were performed using ImageJ, Matlab and Avizo 9.4.

Data availability

Representative samples of the research data are given in the figures. Furthermore, datasets generated and/or analyzed during this study are published on https://doi.org/10.16907/d64d2e8c-b593-47b8-ab90-4ddbd19bedb5.

Received: 22 August 2023; Accepted: 7 September 2023;
Published online: 18 September 2023

References

1. Gisario, A., Kazarian, M., Martina, F. & Mehrpouya, M. Metal additive manufacturing in the commercial aviation industry: a review. *J. Manuf. Syst.* **53**, 124–149 (2019).
2. Blakey-Milner, B. et al. Metal additive manufacturing in aerospace: a review. *Mater. Des.* **209**, 110008 (2021).
3. Awad, A., Fina, F., Goyanes, A., Gaisford, S. & Basit, A. W. Advances in powder bed fusion 3D printing in drug delivery and healthcare. *Adv. Drug Deliv. Rev.* **174**, 406–424 (2021).
4. Diegel, O., Nordin, A. & Motte, D. Additive manufacturing technologies. 19–39 https://doi.org/10.1007/978-981-13-8281-9_2 (2019).
5. Florio, K. et al. An innovative selective laser melting process for hematite-doped aluminum oxide. *Adv. Eng. Mater.* 1801352 https://doi.org/10.1002/adem.201801352 (2019).
6. Juste, E., Petit, F., Lardot, V. & Cambier, F. Shaping of ceramic parts by selective laser melting of powder bed. *J. Mater. Res.* **29**, 2086–2094 (2014).
7. Hagedorn, Y. *Additive Manufacturing of High Performance Oxide Ceramics via Selective Laser Melting* (Fraunhofer Institute of Laser Technologies, 2013).

8. Chen, Z. et al. 3D printing of ceramics: a review. *J. Eur. Ceram. Soc.* **39**, 661–687 (2019).
9. Ivanov, R. A. & Melkikh, A. V. Determination of the optimal mode of laser melting with surface morphology analysis and identification of microstructural defects for created SLM 3D printing parts made of alumina and zirconia stabilized by Yttria. *AIP Conf. Proc.* **2174**, 020105 (2019).
10. Verga, F. et al. Crack-healing, a novel approach for a laser-based powder bed fusion of high-performance ceramic oxides. *Addit. Manuf. Lett.* **1**, 100021 (2021).
11. Wilkes, J., Hagedorn, Y. C., Meiners, W. & Wissenbach, K. Additive manufacturing of ZrO2-Al2O3 ceramic components by selective laser melting. *Rapid Prototyp. J.* **19**, 51–57 (2013).
12. Verga, F. et al. Laser-based powder bed fusion of alumina toughened zirconia. *Addit. Manuf.* **31**, 100959 (2020).
13. Chang, S., Li, L., Lu, L. & Fuh, J. Y. H. Selective laser sintering of porous silica enabled by carbon additive. *Materials* **10**, 1313 (2017).
14. Ferrage, L., Bertrand, G. & Lenormand, P. Dense yttria-stabilized zirconia obtained by direct selective laser sintering. *Addit. Manuf.* **21**, 472–478 (2018).
15. Urruth, G., Maury, D., Voisin, C., Baylac, V. & Grossin, D. Powder bed selective laser processing (sintering/melting) of yttrium stabilized zirconia using carbon-based material (TiC) as absorbance enhancer. *J. Eur. Ceram. Soc.* **42**, 2381–2390 (2022).
16. Makowska, M. et al. Pre-processing of hematite-doped alumina granules for selective laser melting. *Ceram. Int.* **45**, 17014–17022 (2019).
17. Pfeiffer, S. et al. Iron oxide doped spray dried aluminum oxide granules for selective laser sintering and melting of ceramic parts. *Adv. Eng. Mater.* 1801351 https://doi.org/10.1002/adem.201801351 (2019).
18. Pfeiffer, S. et al. Crack-reduced alumina/aluminum titanate composites additive manufactured by laser powder bed fusion of black TiO2-x doped alumina granules. *J. Eur. Ceram. Soc.* https://doi.org/10.1016/j.jeurceramsoc.2022.02.046 (2022).
19. Pfeiffer, S. et al. Selective laser melting of thermal pre-treated METAL oxide doped aluminum oxide granules. *Open Ceram.* 100007 https://doi.org/10.1016/j.oceram.2020.100007 (2020).
20. Haferkamp, L. Effect of the particle size distribution and morphology on powder processability in laser powder bed fusion. https://doi.org/10.3929/ETHZ-B-000549156 (2022).
21. Oliveira, J. P., LaLonde, A. D. & Ma, J. Processing parameters in laser powder bed fusion metal additive manufacturing. *Mater. Des.* **193**, 108762 (2020).
22. Khairallah, S. A., Anderson, A. T., Rubenchik, A. & King, W. E. Laser powder-bed fusion additive manufacturing: physics of complex melt flow and formation mechanisms of pores, spatter, and denudation zones. *Acta Mater.* **108**, 36–45 (2016).
23. Chouhan, A., Aggarwal, A. & Kumar, A. Role of melt flow dynamics on track surface morphology in the L-PBF additive manufacturing process. *Int. J. Heat Mass Transf.* **178**, 121602 (2021).
24. Bayat, M. et al. Keyhole-induced porosities in Laser-based Powder Bed Fusion (L-PBF) of Ti6Al4V: high-fidelity modelling and experimental validation. *Addit. Manuf.* **30**, 100835 (2019).
25. Khairallah, S. A. et al. Controlling interdependent meso-nanosecond dynamics and defect generation in metal 3D printing. *Science* **368**, 660–665 (2020).
26. de Formanoir, C. et al. Micromechanical behavior and thermal stability of a dual-phase α+α' titanium alloy produced by additive manufacturing. *Acta Mater.* **162**, 149–162 (2019).
27. Metelkova, J. et al. On the influence of laser defocusing in selective laser melting of 316L. *Addit. Manuf.* **23**, 161–169 (2018).
28. Chen, M. et al. Microstructural engineering of a dual-phase Ti-Al-V-Fe alloy via in situ alloying during laser powder bed fusion. *Addit. Manuf.* 103173 https://doi.org/10.1016/J.ADDMA.2022.103173 (2022).
29. Withers, P. J. et al. X-ray computed tomography. *Nat. Rev. Methods Prim.* **1**, 1–21 (2021).
30. Du Plessis, A., Yadroitsev, I., Yadroitsava, I. & Le Roux, S. G. X-ray microcomputed tomography in additive manufacturing: a review of the current technology and applications. *3D Print. Addit. Manuf.* **5**, 227–247 (2018).
31. Thompson, A., Maskery, I. & Leach, R. K. X-ray computed tomography for additive manufacturing: a review. *Meas. Sci. Technol.* **27**, 072001 (2016).
32. Ghasemi-Tabasi, H. et al. Mapping spatial distribution of pores in an additively manufactured gold alloy using neutron microtomography. *Appl. Sci.* **11**, 1512 (2021).
33. Gunenthiram, V. et al. Experimental analysis of spatter generation and melt-pool behavior during the powder bed laser beam melting process. *J. Mater. Process. Technol.* **251**, 376–386 (2018).
34. Parab, N. D. et al. High-speed synchrotron X-ray imaging of laser powder bed fusion. *Processes* **32**, 4–8 (2019).
35. Hooper, P. A. Melt pool temperature and cooling rates in laser powder bed fusion. *Addit. Manuf.* **22**, 548–559 (2018).
36. Sun, T., Tan, W., Chen, L. & Rollett, A. In situ/operando synchrotron x-ray studies of metal additive manufacturing. *MRS Bull.* **45**, 927–933 (2020).
37. Hocine, S., Van Swygenhoven, H. & Van Petegem, S. Verification of selective laser melting heat source models with operando X-ray diffraction data. *Addit. Manuf.* **37**, 101747 (2021).
38. Hocine, S. et al. A miniaturized selective laser melting device for operando X-ray diffraction studies. *Addit. Manuf.* **34**, 101194 (2020).
39. Ghasemi-Tabasi, H. et al. Direct observation of crack formation mechanisms with operando Laser Powder Bed Fusion X-ray imaging. *Addit. Manuf.* 102619 https://doi.org/10.1016/J.ADDMA.2022.102619 (2022).
40. Chen, M. et al. A quantitative study of thermal cycling along the build direction of Ti-6Al-4V produced by laser powder bed fusion. *Mater. Des.* **225**, 111458 (2023).
41. Calta, N. P. et al. An instrument for in situ time-resolved X-ray imaging and diffraction of laser powder bed fusion additive manufacturing processes. *Rev. Sci. Instrum.* **89**, 055101 (2018).
42. Martin, A. A. et al. Dynamics of pore formation during laser powder bed fusion additive manufacturing. *Nat. Commun.* **10**, 1–10 (2019).
43. Martin, A. A. et al. Ultrafast dynamics of laser-metal interactions in additive manufacturing alloys captured by in situ X-ray imaging. *Mater. Today Adv.* **1**, 100002 (2019).
44. Karagadde, S., Leung, C. L. A. & Lee, P. D. Progress on in situ and operando X-ray imaging of solidification processes. *Materials* **14**, 2374 (2021).
45. Chen, Y. et al. In situ X-ray quantification of melt pool behaviour during directed energy deposition additive manufacturing of stainless steel. *Mater. Lett.* **286**, 129205 (2021).
46. Leung, C. L. A. et al. Laser-matter interactions in additive manufacturing of stainless steel SS316L and 13-93 bioactive glass revealed by in situ X-ray imaging. *Addit. Manuf.* **24**, 647–657 (2018).
47. Sinclair, L. et al. In situ radiographic and ex situ tomographic analysis of pore interactions during multilayer builds in laser powder bed fusion. *Addit. Manuf.* **36**, 101512 (2020).
48. Glerum, J. A., Kenel, C., Sun, T. & Dunand, D. C. Synthesis of precipitation-strengthened Al-Sc, Al-Zr and Al-Sc-Zr alloys via selective laser melting of elemental powder blends. *Addit. Manuf.* **36**, 101461 (2020).
49. Zhao, C. et al. Real-time monitoring of laser powder bed fusion process using high-speed X-ray imaging and diffraction. *Sci. Rep.* **7**, 3602 (2017).
50. Kouraytem, N. et al. Effect of laser-matter interaction on molten pool flow and keyhole dynamics. *Phys. Rev. Appl.* **11**, 064054 (2019).
51. Leung, C. L. A. et al. In situ X-ray imaging of defect and molten pool dynamics in laser additive manufacturing. *Nat. Commun.* **9**, 1355 (2018).
52. Cunningham, R. et al. Keyhole threshold and morphology in laser melting revealed by ultrahigh-speed x-ray imaging. *Science* **363**, 849–852 (2019).
53. Kouraytem, N. et al. Solidification crack propagation and morphology dependence on processing parameters in AA6061 from ultra-high-speed x-ray visualization. *Addit. Manuf.* **42**, 101959 (2021).
54. Wang, L., Zhang, Y., Chia, H. Y. & Yan, W. Mechanism of keyhole pore formation in metal additive manufacturing. *npj Comput. Mater.* **8**, 1–11 (2022).
55. Hojjatzadeh, S. M. H. et al. Direct observation of pore formation mechanisms during LPBF additive manufacturing process and high energy density laser welding. *Int. J. Mach. Tools Manuf.* **153**, 103555 (2020).
56. Zhao, C. et al. Critical instability at moving keyhole tip generates porosity in laser melting. *Science* **370**, 1080–1086 (2020).
57. Qu, M. et al. Controlling process instability for defect lean metal additive manufacturing. *Nat. Commun.* **13**, 1–8 (2022).
58. García-Moreno, F. et al. Tomoscopy: time-resolved tomography for dynamic processes in materials. *Adv. Mater.* **33**, 2104659 (2021).
59. García-Moreno, F. et al. Using X-ray tomoscopy to explore the dynamics of foaming metal. *Nat. Commun.* **10**, 1–9 (2019).
60. Marone, F. et al. Time resolved in situ X-ray tomographic microscopy unraveling dynamic processes in geologic systems. *Front. Earth Sci.* **7**, 346 (2020).
61. Florio, K. et al. Process characterization and analysis of ceramic powder bed fusion. *Int. J. Adv. Manuf. Technol.* **117**, 2105–2116 (2021).
62. Kirshenbaum, A. D. & Cahill, J. A. The density of liquid aluminium oxide. *J. Inorg. Nucl. Chem.* **14**, 283–287 (1960).
63. Guo, Q. et al. In-situ full-field mapping of melt flow dynamics in laser metal additive manufacturing. *Addit. Manuf.* **31**, 100939 (2020).
64. Rehman, A. U., Pitir, F. & Salamci, M. U. Full-field mapping and flow quantification of melt pool dynamics in laser powder bed fusion of SS316L. *Materials* **14**, 6264 (2021).
65. Patnaik, P. *Handbook of Inorganic Chemicals Pradyot* s8-X, 192 (McGraw-Hill, 2003).
66. Paradis, P. F. & Ishikawa, T. Surface tension and viscosity measurements of liquid and undercooled alumina by containerless techniques. *Jpn. J. Appl. Phys.* **44**, 5082–5085 (2005).

67. Cullom, T. et al. Frequency domain measurements of melt pool recoil force using modal analysis. *Sci. Rep.* **11**, 1–11 (2021).
68. Chen, Y. et al. In-situ synchrotron imaging of keyhole mode multi-layer laser powder bed fusion additive manufacturing. *Appl. Mater. Today* **20**, 100650 (2020).
69. Courtois, M. et al. A complete model of keyhole and melt pool dynamics to analyze instabilities and collapse during laser welding. *J. Laser Appl.* **26**, 042001 (2014).
70. King, W. E. et al. Observation of keyhole-mode laser melting in laser powder-bed fusion additive manufacturing. *J. Mater. Process. Technol.* **214**, 2915–2925 (2014).
71. Naderi, M., Weaver, J., Deisenroth, D., Iyyer, N. & McCauley, R. On the fidelity of the scaling laws for melt pool depth analysis during laser powder bed fusion. *Integr. Mater. Manuf. Innov.* **12**, 11–26 (2022).
72. Hann, D. B., Iammi, J. & Folkes, J. A simple methodology for predicting laser-weld properties from material and laser parameters. *J. Phys. D Appl. Phys.* **44**, 445401 (2011).
73. Florio, K. Powder bed fusion of ceramic oxides: process development and process understanding. https://doi.org/10.3929/ETHZ-B-000544358 (2022).
74. Touloukian, Y. S., Saxena, S. C. & Hestermans, P. *Viscosity*—Google Books. https://books.google.ch/books?id=iHnTnQEACAAJ&source=gbs_book_other_versions (2013).
75. Mokso, R. et al. GigaFRoST: the gigabit fast readout system for tomography. *J. Synchrotron Radiat.* **24**, 1250–1259 (2017).
76. Marone, F. & Stampanoni, M. Regridding reconstruction algorithm for real-time tomographic imaging. *J. Synchrotron Radiat.* **19**, 1029–1037 (2012).
77. Application: LFA 1000—Aluminium oxide—Thermal diffusivity. https://www.linseis.com/en/applications/ceramics-and-glass-industry/lfa-1000-aluminum-oxide-al2o3-thermal-diffusivity-conductivity/.
78. Auerkari, P. *Mechanical and Physical Properties of Engineering Alumina Ceramics* (VTT Technical Research Centre of Finland, 1996).
79. Chase, M. W. J. *NIST-JANAF Thermochemical Tables 2 Volume-Set (Journal of Physical and Chemical Reference Data Monographs)*, Vol. 9, 1–1951 (American Institute of Physics, 1998).

Acknowledgements

This research work was mainly supported by the Swiss National Science Foundation with a grant CRSK-2_196085. The authors acknowledge the Paul Scherrer Institut, Villigen, Switzerland for provision of synchrotron radiation beamtime at the TOMCAT beamline of the SLS. Moreover, the authors gratefully thank Prof. Helena Van Swygenhoven for fruitful discussions and advisory. The authors acknowledge the ETH Board for funding the SFA FUORCLAM project within the frame of the SFA (Strategic Focus Areas) Advanced Manufacturing, which supported the presented research.

Author contributions

M.G.M. acquired funding (SNF CRSK-2_196085), designed the research and supervised the project. M.G.M., F.V. and K.F. designed and developed the LPBF operando setup. S.P. optimized and synthesized the powder. F.M. and C.M.S. developed the beamline setup, characterization and tomography reconstruction method. M.G.M., F.V., S.V.P. and C.S.T.C. developed the measurement procedures, performed operando tomography and acquired data. M.G.M. analyzed the experimental data. M.G.M., F.V. and S.V.P. contributed to data interpretation and wrote the manuscript, with contributions from all authors. K.W. and T.G. acquired funding (SFA Fuorclam) and provided experimental infrastructure. All authors supported revising the manuscript.

Competing interests

The authors declare no competing interests.

Additional information

Supplementary information The online version contains supplementary material available at https://doi.org/10.1038/s43246-023-00401-3.

Correspondence and requests for materials should be addressed to Malgorzata G. Makowska or Steven Van Petegem.

Peer review information *Communications Materials* thanks the anonymous reviewers for their contribution to the peer review of this work. Primary Handling Editor: John Plummer. A peer review file is available.

Reprints and permission information is available at http://www.nature.com/reprints

Publisher's note Springer Nature remains neutral with regard to jurisdictional claims in published maps and institutional affiliations.

Open Access This article is licensed under a Creative Commons Attribution 4.0 International License, which permits use, sharing, adaptation, distribution and reproduction in any medium or format, as long as you give appropriate credit to the original author(s) and the source, provide a link to the Creative Commons licence, and indicate if changes were made. The images or other third party material in this article are included in the article's Creative Commons licence, unless indicated otherwise in a credit line to the material. If material is not included in the article's Creative Commons licence and your intended use is not permitted by statutory regulation or exceeds the permitted use, you will need to obtain permission directly from the copyright holder. To view a copy of this licence, visit http://creativecommons.org/licenses/by/4.0/.

© The Author(s) 2023